BODIPY modified g-C$_3$N$_4$ as a highly efficient photocatalyst for degradation of Rhodamine B under visible light irradiation

De-Gao Wang, Pengfei Tan, Huan Wang, Min Song, Jun Pan, Gui-Chao Kuang*

State Key Laboratory of Power metallurgy, Central South University, Lushan South Road 932, Yuelu District, Changsha, Hunan 410083, PR China

共同一作

ARTICLE INFO

ABSTRACT

Developing new energy resource as well as efficient treatment strategies to solve the energy crisis and organic pollutants problems is of crucial importance. Due to medium band gap and highly thermal stability, doped or chemically functionallized graphitic carbon nitride (g-C$_3$N$_4$) has been envisioned as promising photocatalysts in processing organic pollutants. In this work, we use 4,4-difluoro-4-bora-3a,4a-diaza-s-indacene (BODIPY) chemically modified g-C$_3$N$_4$ to degrade Rhodamine B (RhB) under visible light irradiation ($\lambda \geq 420$ nm). When the modified weight ratio of BODIPY in g-C$_3$N$_4$ reaches 0.6% (**CN-0.6**), the photocatalytic performance is nearly 3.5 times fast than that of without modification (**CN-0**). Enhanced visible light absorption and depressed electron-hole recombination rate may take responsibilities for the enhanced photocalytic performance. A possible mechanism responsible for this photocatalytic process is proposed. Our work might provide a new strategy to develop valid photocatalysts with broad visible light absorption.

1. Introduction

Dye-containing wastewater has gained considerable attention in the last decades due to their adverse effects on environment and human health [1]. These organic dyes are complex aromatic compounds and resistant to degradation [2,3]. Especially, Rhodamine B (RhB), which has been proved one kind of carcinogenic compounds but widely used in leather, paper and textiles fields, might cause serious toxicities to public health [4]. Therefore, developing efficient strategies to degrade RhB from water is impending.

Graphitic carbon nitride (g-C$_3$N$_4$) has shown its priorities in pollutant degradation due to its low cost, metal free, excellent thermal and chemical stability and expediently structural modification [5–9]. However, the photocatalytic performance of g-C$_3$N$_4$ is impaired by fast charge recombination and narrow visible light absorption region [10–13]. Therefore, growing work has been done to the dope or chemically functionalize g-C$_3$N$_4$ to tune the lowest unoccupied molecular orbital (LUMO) and highest occupied molecular orbital (HOMO), and thus to optimize the photocatalytic activities [14–22]. In fact, attaching long wavelength absorption dyes would improve the visible light response of g-C$_3$N$_4$ based photocatalysts.

We initiated the research program on BODIPY and its derivatives since 2013 and investigated their photophysical and porous properties with various molecular architectures [23–28]. Although various of dyes have been successfully doped to improve the photocatalytic activities of

g-C$_3$N$_4$, there is rare work referred to BODIPY chemically modified g-C$_3$N$_4$ while this dye has been well investigated due to its excellent photophysical properties [29]. In this work, we utilized the BODIPY derivatives to chemically react with the residual amine on g-C$_3$N$_4$ frameworks with different ratios. With different ratio of BODIPY derivatives addition, their photophysical properties and corresponding photodegradation ability for RhB were compared. The promising results demonstrated that rational ratio of chemical doping BODIPY dyes could greatly enhance visible light absorption and improve photocatalytic performance.

2. Experimental section

### 2.1. Materials and equipments

All the chemical reagents were commercial available and used as received unless otherwise stated. Dichloromethane (DCM) was dried using CaCl$_2$. All reactions were performed under nitrogen atmosphere. Flash column chromatography was performed using 40–63 µm (230–400 mesh) silica gels as the stationary phase.

2.2. Synthesis of g-C$_3$N$_4$ (CN-0)

The porous **CN-0** was prepared through direct heating urea in ceramic crucible with a cover in air. In a typical process, urea (8.0 g)
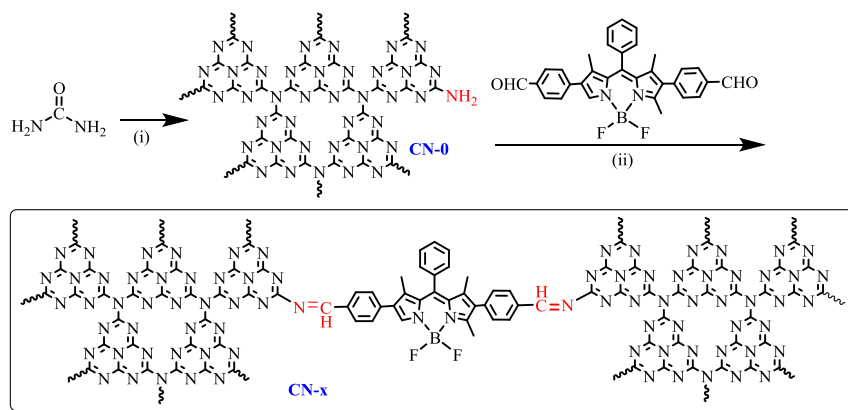
Scheme 1. Synthetic route for **CN-x** (x = 0, 0.1, 0.3, 0.6, 0.9 and 1.2, respectively). (i) 500 °C, 4 h; (ii) **BDP-2CHO**, 1,4-dioxane, acetic acid, 110 °C, 2 h.

was put into a crucible and then was heated to 500 °C with a heating rate of 2.3 °C/min. The sample was kept at 500 °C for 4 h in a muffle furnace. The acquired solid was washed, dried and collected for further usage.

2.3. Synthesis of CN-x by post modification of the CN-0

Synthesis of **CN-x** (x = 0, 0.1, 0.3, 0.6, 0.9 and 1.2) was according to literature (Scheme 1) [29]. **CN-x** were prepared by Schiff base reaction between **CN-0** and different weight fraction di-aldehyde using acetic acid as catalyst. The weight fraction of di-aldehyde varied from 0% to 1.2% for **CN-x** (x = 0, 0.1, 0.3, 0.6, 0.9 and 1.2). Herein, we took the synthesis of **CN-0.1** as an example to give details about the synthetic process. Under N_2 atmosphere, **CN-0** (100 mg) and **BDP-2CHO** (0.1 mg) were dispersed in 1,4-dioxane (6 mL). When the solution refluxed, acetic acid (0.6 mL) was added dropwise. The solution refluxed for another 2 h before cooling down. Then the solvents were removed by vacuum rotary and the residue was washed by organic solvents (DCM and methanol, 2 h, respectively) and water. The resultant powder was freeze-dried prior to use.

2.4. Characterization

Crystal structure of **CN-x** (x = 0, 0.1, 0.3, 0.6, 0.9 and 1.2) was investigated by X-Ray diffraction XRD using Rigaku diffractometer of Cu target with Kα = 0.15405 nm. Measurements were collected in the angles range from 10° to 70° at scan rate of 5°/min. UV–vis absorption spectra and photoluminescence (PL) measurements were measured using Hitachi U-5100 and Hitachi F-2700, respectively. Fourier transform infrared (FT-IR) spectra were obtained on a Nicolet 6700 and reported in terms of the frequency of absorption (cm^{-1}). X-ray photoelectron spectroscopy (XPS) analysis was performed on an ESCALab MKII X-ray photoelectron spectrometer using Mg-Kα radiation. Scanning electron microscopy (SEM) images and element mapping measurements were performed on a FEI SIRION200 microscopy. Transmission electron microscopy (TEM) tests were performed on a JEOL JEM-2100F microscopy. According to the absorption-desorption isotherms, BET (Brunauer–Emmett–Teller) specific surface area, pore size distribution and pore volume were evaluated. Before each measurement, the samples were degassed at 120 °C for 6 h.

2.5. Photocatalytic activity test

The photocatalytic activities were evaluated under a 300 W Xe lamp with a 420 nm cut-off filter. In every experiment, photocatalyst (10 mg) was placed in a quartz tube containing RhB solution (15 mL, 10 mg L^{-1}). Prior to irradiation, the suspension was magnetically stirred for 30 min in the dark to ensure that the RhB could reach adsorption/

desorption equilibrium on the photocatalyst surface. After irradiation, the solution (5 mL) was suctioned at a regular time interval and centrifuged to remove the precipitates, then the concentrations of RhB in the supernatant was determined by a UV–vis spectrophotometer at a wavelength of 554 nm. The trapping experiments concerning active species in the photocatalytic process were also conducted by adding the different scavengers to the RhB solution prior to the photocatalysis in the similar procedure.

2.6. Photoelectrochemical measurements

The photocurrent was measured on CHI660e electrochemical workstation by using a standard three-electrode system. A platinum plate electrode, standard calomel electrode in saturated KCl and the as-prepared catalysts were used as the counter electrode, the reference electrode and working electrode, respectively. Sodium sulfate aqueous solution (0.1 M) was acted as electrolyte. Electrochemical impedance spectroscopy (EIS) was investigated at 5 mV amplitude. The frequency range was from 0.1 to 1000 kHz by using a three-electrode system in sodium sulfate solution (0.1 M). To prepare the working electrode, photocatalyst (10 mg) was dispersed into water (1 mL) containing Nafion aqueous solution (20 μL, 5 wt%). After ultrasonic treatment for 30 min, the suspension was dip-coated for several times onto a $1 \times 1\ cm^2$ indium tin oxide (ITO) glass. For each measurement, the conductive glass was dried at 60 °C for 30 min before next cycle.

3. Results and discussion

The synthesis of **BDP-2CHO** was according to literature (Scheme 1) [23]. During the synthesis of **CN**, amine groups were left at the end of s-triazine rings because of kinetic problems [30]. Consequently, **BDP-2CHO** can react with residual amine groups and then incorporate into the conjugated system. After reaction, the obtained **CN-x** was washed by organic solvents and water. The samples were freeze-dried for 24 h prior to use.

As the BODIPY dye addition would greatly improve the photocatalytic abilities of the g-C_3N_4, we prepared a series of modified g-C_3N_4 with varying **BDP-2CHO** weight ratio to optimize the photocatalytic abilities. Characterization techniques such as FT-IR, XPS, XRD, and electron microscopy were used to investigate the structural and morphological information.

SEM mapping tests were performed to detect the degree of BODIPY modification and the boron element was chosen as a characteristic element. The boron element intensities increase gradually as the fraction improvement **BDP-2CHO** (Fig. S1). FT-IR spectra of the as-prepared samples proved the Schiff base formation (Fig. 1). For **BDP-2CHO**, absorption peaks at 2846, 2733 and 1727 cm^{-1} were ascribed to C–H and C=O stretching vibration, respectively. The peaks at 1549,
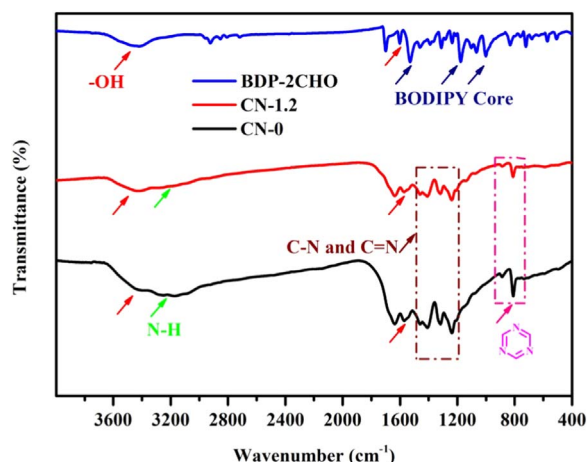
Fig. 1. FT-IR spectra of **BDP-2CHO**, **CN-0** and **CN-1.2**.

1200 and 1005 cm^{-1} were characteristic absorption of the BODIPY moieties [24–26]. Typical absorption bands revealing the structures of **CN** were exhibited in **CN-1.2**. Peaks near 3500 and 1600 cm^{-1}, which were attributed to the −OH stretching vibration, resulted from the aqueous oxide absorption by **CN-x**. The peak around 3200 cm^{-1} was attributed to the N−H stretching vibration [31]. The absorption of N−H (3100–3400 cm^{-1}) decreased as the decoration content of **BDP-2CHO**, indicating the decreased content of surface amino groups in **CN-x** (Fig. S2a). The adsorption band near 1506 cm^{-1} attributed to aromatic C=C bonds can't be found in our FT-IR results even the weight ratio of **BDP-2CHO** reached 1.2 wt%. (Fig. S2b). The multiple bands between 1200 and 1650 were characteristic absorption bands ascribed to C-N and C=N stretching vibration (the wine color dotted region) [10]. Peaks near 860 and 800 resulted from the stretching vibration of the *s*-triazine rings vibrations (the magenta color dotted region) [32].

The crystalline structure of **CN-x** was investigated by XRD measurement (Fig. S3). Typical peaks of pure *g*-C$_3$N$_4$ were at about 13.2° and 27.4°, belonging to (100) and (002) diffraction planes. Compared with **CN-0**, the (002) diffraction peaks of the **CN-x** exhibit a little upfield as increasing ratio of BODIPY derivatives. These results might be from the Schiff base linkage between the edges of the *g*-C$_3$N$_4$. More BODIPY chemically attachment between the residual amine groups would induce more constriction of crystal lattice for *g*-C$_3$N$_4$.

Porous properties of **CN-x** were evaluated by absorption/desorption analysis under 77 K (Fig. S4). **CN-x** showed typical type IV isotherms according to IUPAC classification indicating mesoporous properties of **CN-x**. The pore size delivered a wide distribution mainly between 0 and 55 nm, which came from the meso-porous properties of the photocatalysts and accumulation of the plate-like structures (Figs. S5, S6). The Brunauer−Emmett−Teller (BET) surface areas for **CN-x** were 58, 70, 78, 82, 70 and 57 m^2 g^{-1}, respectively, which indicated that **BDP-2CHO** modification had little effect on the pure **CN-0** porous properties.

Diffuse reflectance spectra (DRS, Fig. 2a) were performed for **CN-x** before the photocatalytic tests. Contrary to little changes were detected when the BODIPY weight fraction was less than 0.3 wt% (**CN-0**, **0.1**, **0.3**), the spectra showed obvious absorption enhancement on the visible light region and underwent red shift after the content exceed 0.6 wt%. Two reasons might be responsible for this variation [33,34]. First, incorporation of the **BDP-2CHO** extended the conjugated degree of the *g*-C$_3$N$_4$. Second, some of the *g*-C$_3$N$_4$ interlayer might be tortuous by the Schiff base linkage. Therefore, the electron transition from *n* to *π** orbital would be activated. Finally, strengthened light absorption and red-shifted light absorption endowed the as-prepared photocatalysts enhanced utilization of the light.

Photoluminescence spectra (PL) was widely employed to determine

the migration and recombination process of the photo-induced electron-hole pairs [35]. In this work, PL spectra of the **CN-x** were acquired under room temperature with an excitation wavelength of 370 nm (Fig. 2b). **CN-x** showed same emission maximum wavelength but different emission intensities. For **CN-x** (x = 0. 0.1, 0.3 and 0.6), the emission intensities were gradually decreased first and then dramatically fall for **CN-0.6**. When more BODIPY moieties were incorporated for **CN-0.9** and **CN-1.2**, the emission intensities would be restored gradually which inferred that the recombination of charge carriers were suppressed after decoration. The suppressed contents were dependent on the weight ratio of BODIPY moieties. In this condition, the **CN-0.6** might be the best one to adsorb the photons for photocatalytic application [36].

The charge transfer rate of the **CN-0.6** and **CN-0** were compared by performing electrochemical impedance spectra (EIS) tests (Fig. 3). The arc radius of **CN-0.6** was smaller than that of **CN-0**, indicating **CN-0.6** had a faster interfacial charge transfer and a more effective separation of carriers. The charge separation and migration could significantly affect the photocatalytic performance, which could be verified by the photocurrent response. In this study, the photocurrent−time (i−t) curves of **CN-0.6** and **CN-0** working electrodes were conducted with several 20 s light on/off under visible light irradiation. The photocurrent density for **CN-0.6** was much higher than that of **CN-0**, suggesting a distinct improvement in the suppression of photogenerated electron−hole recombination, and this result was consistent with the latter photocatalytic degradation of RhB.

The photocatalytic capabilities of the as-prepared composites were investigated by the decomposition of RhB under visible light irradiation (Fig. 4a). To investigate the amount of RhB adsorbed under dark, we added the RhB adsorption spectra under dark condition in the presence of **CN-x** for 30 min and the adsorption equilibrium can be achieved within the initial contact time of 20 min (Fig. S7). In the control experiment, the self-degradation of RhB was almost negligible without photocatalyst and **CN-0** also shown an obviously low efficiency to degrade RhB (ca. 28%) after irradiation of 30 min while modification with a small amount of BODIPY moieties on the surface of **CN** could dramatically improve the photocatalytic performances. Results showed the weight ratio of BODIPY moieties on **CN** was crucial to the photocatalytic activities. **CN-0.6** exhibited best photocatalytic abilities and would degrade RhB totally in the solution under the same condition, nearly 3.5 times fast than that of **CN-0**. When the BODIPY weight ratio exceeded 0.6 wt%, the photocatalytic activities decreased, which might be from the less visible light absorption by *g*-C$_3$N$_4$ for the high absorption of BODIPY dye.

To give deep insights of the photocatalytic process, experimental results were simulated by pseudo first-order kinetic model and listed in Fig. 4b. The photocatalytic process fitted well with a pseudo-first-order model.

$$ln(C_o/C) = kt$$

Where *k* is the apparent kinetic rate constants, *t* is the reaction time; *C* and *C*$_o$ are the concentration at *t* and the initial concentration of the organic dyes, respectively. The *k* values for RhB degradation with **CN-0** was 1.1% min^{-1}. For BODIPY-modified *g*-C$_3$N$_4$, composites with **BDP-2CHO** of 0.6 wt% exhibited best photocatalytic performance, and the decomposition rate constants were calculated to be 12.8% min^{-1} (Fig. 4c). The results demonstrated that the introduction of BODIPY into *g*-C$_3$N$_4$ accelerated the photocatalytic degradation rate. Finally, we compared photocatalytic abilities of **CN-0.6** with that of TiO$_2$ in the references (Table S1). From this comparison, our photocatalysts delivered superiorities than the reported TiO$_2$ in degradation of organic dyes.

Cycling performances for **CN-x** were evaluated (Fig. 4d). The recycled **CN-0** and **CN-0.6** were collected through high-speed centrifugation, water washed and dried. After that, the reused samples (10 mg) were hanged on to use for the next degradation process. **CN-0**
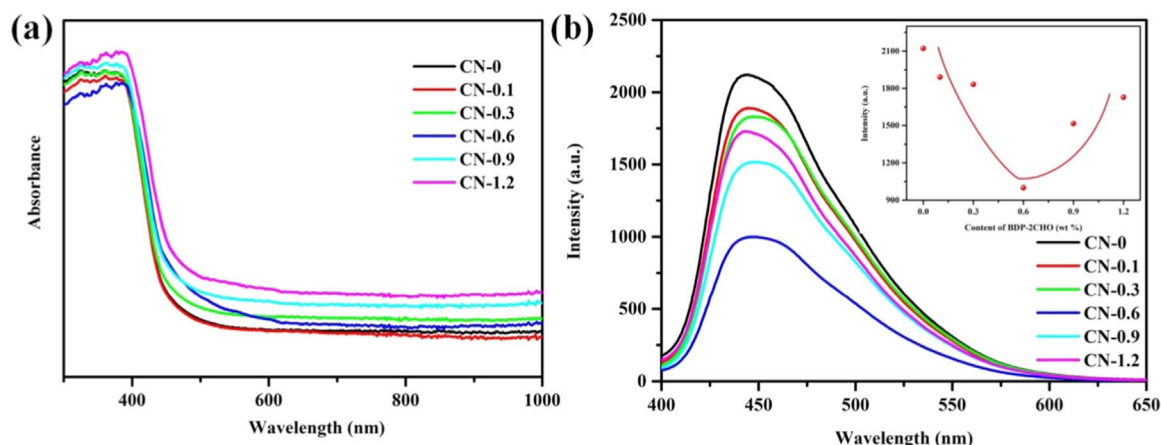
Fig. 2. (a) DRS and (b) fluorescence spectra of the as-prepared photocatalysts **CN-x** (x = 0, 0.1, 0.3, 0.6, 0.9 and 1.2, respectively).
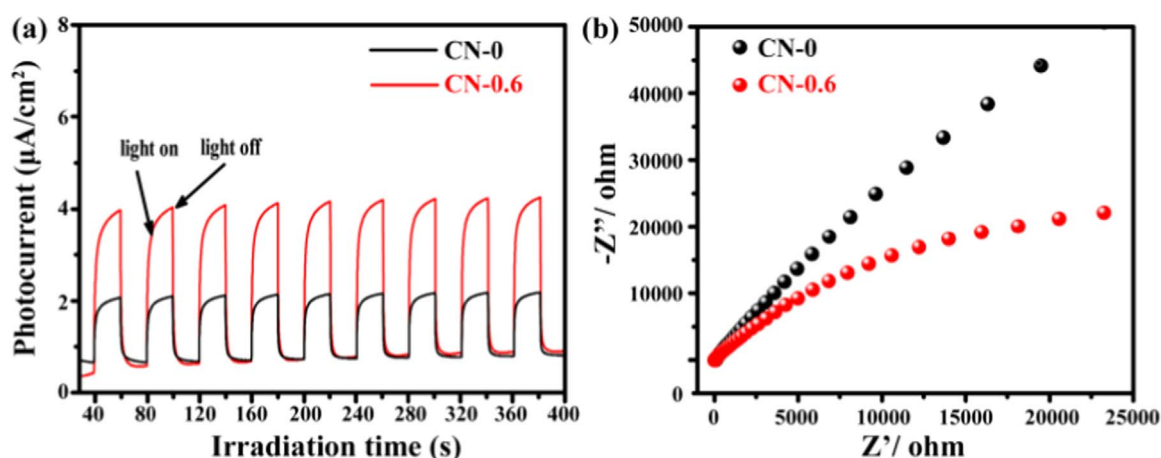

Fig. 3. (a) The photocurrent and (b) electrochemical impedance spectroscopies of **CN-0** and **CN-0.6**.

photocatalytic performance showed slight drop. While for **CN-0.6**, the photocatalytic degradation abilities for RhB displayed no change even after four recycle experiments indicating **CN-0.6** was endowed with good cyclic performance.

XRD, SEM and TEM experiments were carried out to investigate the structure stabilities of the collected **CN-0.6** after four cyclic experiments (Fig. S8). The reused **CN-0.6** possessed same crystalline structures because no new diffraction peaks appeared, demonstrating this photocatalyst possessed high structural stability. Further morphological investigation from SEM and TEM revealed no obvious changes. Therefore, our results indicated that **CN-0.6** not only possessed well RhB cyclic degradation performance, but also displayed high structural stability.

Active trapping experiments were performed to investigate the main active species during the degradation process and the probable photocatalytic mechanism (Fig. 5). Ethylenediamine tetraacetic acid disodium salt (EDTA-2Na, 5 mM), p-benzoquinone (BZQ, 5 mM) and tert-butyl alcohol (TBA, 10 mM) were adopted as scavengers for photo-generated holes (h^+), superoxide radical ($\cdot O_2^-$) and hydroxyl radical ($\cdot OH$), respectively. All the degradation experiments of RhB using **CN-0.6** were conducted in the same condition as aforementioned, except that the scavenger was added separately. The degradation efficiency was slightly suppressed upon addition of TBA. In contrast, the degradation rates dramatically decreased after the appearance of EDTA-2Na or BQ, implying that the active species h^+ and $\cdot O_2^-$ have strong effects than $\cdot OH$ on the photocatalytic process.

Based on the experimental results and previous contributions

[37,38], we proposed a possible degradation mechanism for BODIPY-g-C_3N_4 (Fig. 6). Under visible light irradiation, both the BODIPY and g-C_3N_4 absorbed photons and thus simultaneously generated corresponding electron−hole pairs. Considering the LUMO of the BODIPY is a little bit higher than that of g-C_3N_4 and the electron transfer theory, the excited electron would transfer to the excited of conduction band (CB) of g-C_3N_4. Actually, the electron transfer would greatly suppress the electron-hole recombination in BODIPY. And more excited electrons would gather in the conduction band of g-C_3N_4 to take part in photocatalytic process. Meanwhile, the electron transfer would greatly depress the electron−hole recombination in the g-C_3N_4. The holes interact with water forming the hydroxyl radical ($\cdot OH$) and proton ($H\cdot$) reactive species while the electron interact with the O_2 generating the superoxide radical ($\cdot O_2^-$). The $H\cdot$ species are not stable and interact with $\cdot O_2^-$ forming the $O_2H\cdot$. Finally, RhB was degraded by the $\cdot OH$ and $O_2H\cdot$ radicals producing color-less compounds organic (CCO), carbon dioxide (CO_2) and water as shown in Fig. 6.

4. Conclusions

In conclusion, chemically modified g-C_3N_4 frameworks were successfully obtained utilizing Schiff base reaction with BODIPY dyes. Results revealed that small weight ratio of this dye would dramatically enhance the composite's degradation ability of RhB under visible light irradiation. Further photocatalytic porous polymers for hydrogen generation from water are underway in our laboratory and will be reported in due course.
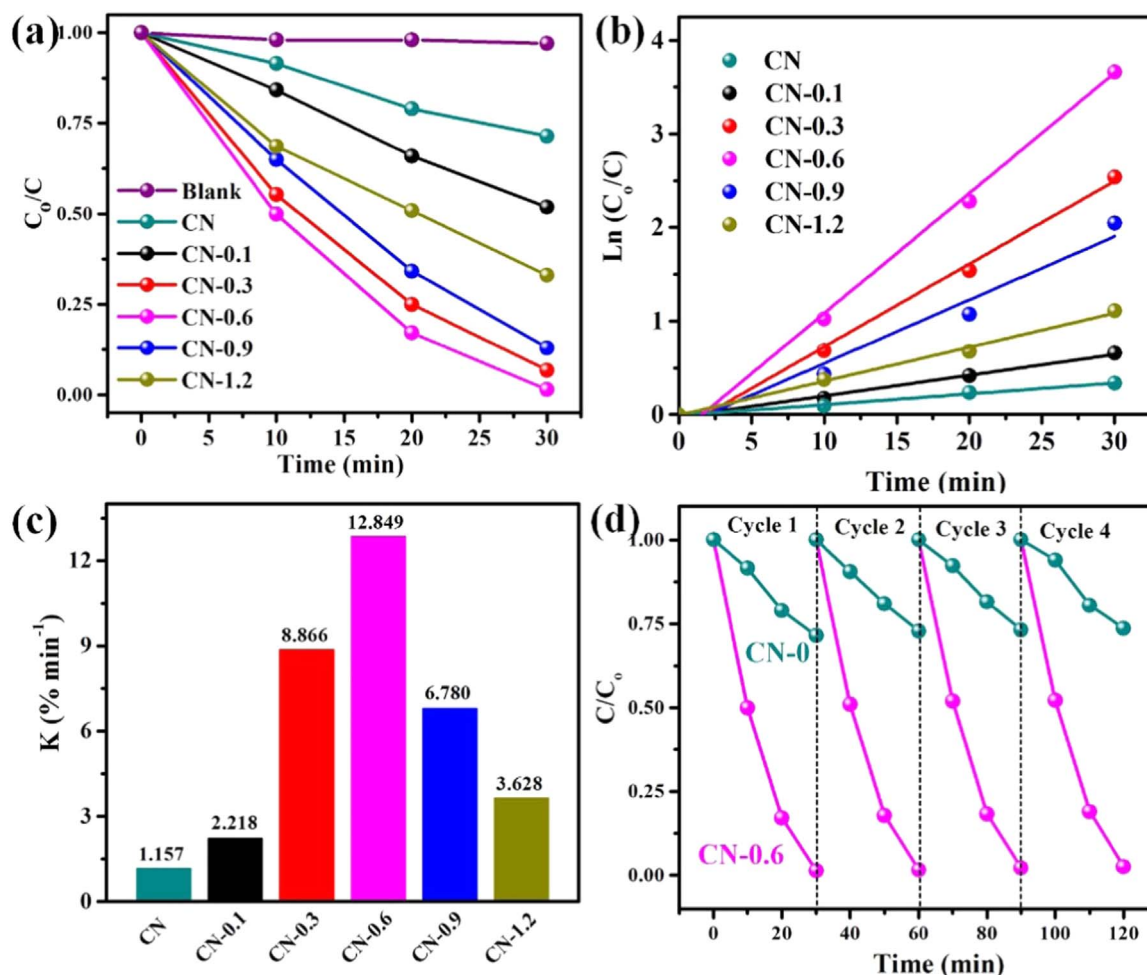
Fig. 4. (a) The photocatalytic activity of the samples for RhB solution, (b) the kinetics plots of RhB degradation over the as-synthesized photocatalysts, (c) the apparent rate constant over all samples and (d) cyclic degradation tests for degradation of RhB under visible light ($\lambda \geq 420$ nm) irradiation.
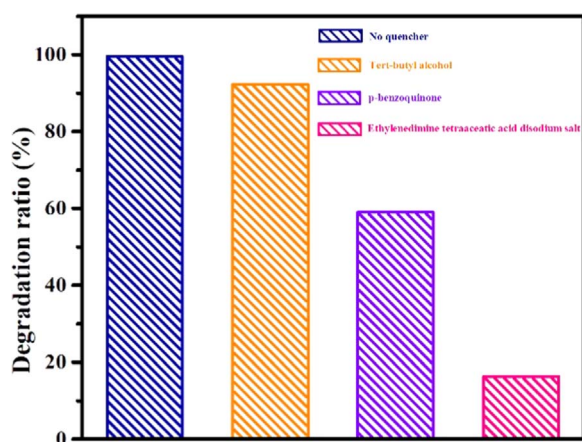

Fig. 5. Photocatalytic activities of **CN-0.6** for the degradation of RhB in the presence of different scavengers.
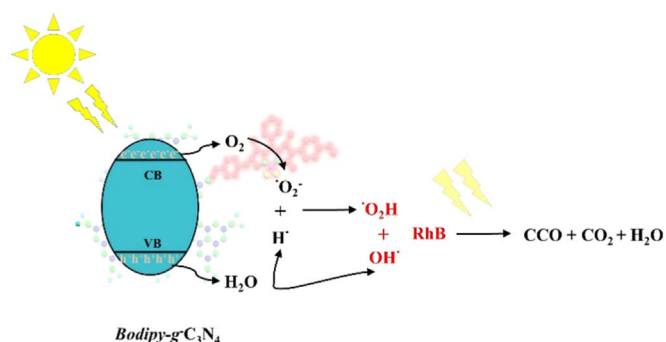

Fig. 6. Proposed degradation mechanism of RhB using BODIPY-*g*-C_3N_4.

was written through contributions from all the authors. All authors have given approval to the final version of the manuscript.

Conflicts of interest

There are no conflicts of interest to declare.

Author contributions

De-Gao Wang and Pengfei Tan contributed equally. The manuscript

共同一作

Appendix A. Supporting information

Supplementary data associated with this article can be found in the online version at doi:10.1016/j.jssc.2018.08.002.

References

[1] S. Cao, J. Low, J. Yu, M. Jaroniec, Polymeric photocatalysts based on graphitic carbon nitride, Adv. Mater. 27 (2015) 2150–2176.

[2] I.I. Savin, R. Butnaru, Waste water characteristics in textile finishing mills, Environ. Eng. Manag. J. 7 (2008) 859–864.

[3] K.Y. Foo, B.H. Hameed, Decontamination of textile waste water via TiO_2/activated carbon composite materials, Adv. Colloid Interface Sci. 159 (2010) 130–143.

[4] R. Jain, M. Mathur, S. Sikarwar, A. Mittal, Removal of the hazardous dye rhodamine B through photocatalytic and adsorption treatments, J. Environ. Manag. 85 (2007) 956–964.

[5] W.-J. Ong, L.-L. Tan, Y.H. Ng, S.-T. Yong, S.-P. Chai, Graphitic carbon nitride (*g*-C_3N_4)-based photocatalysts for artificial photosynthesis and environmental remediation: are we a step closer to achieving sustainability?, Chem. Rev. 116 (2016) 7159–7329.

[6] G. Mamba, A.K. Mishra, Graphitic carbon nitride (*g*-C_3N_4) nanocomposites: a new and exciting generation of visible light driven photocatalysts for environmental pollution remediation, Appl. Catal. B 198 (2016) 347–377.

[7] Y. Zheng, L. Lin, B. Wang, X. Wang, Graphitic carbon nitride polymers toward sustainable photoredox catalysis, Angew. Chem. Int. Ed. 54 (2015) 12868–12884.

[8] Y. Wang, X. Wang, M. Antonietti, Polymeric graphitic carbon nitride as a heterogeneous organocatalyst: from photochemistry to multipurpose catalysis to sustainable chemistry, Angew. Chem. Int. Ed. 51 (2012) 68–89.

[9] Y. Zheng, J. Liu, J. Liang, M. Jaroniec, S.Z. Qiao, Graphitic carbon nitride materials: controllable synthesis and applications in fuel cells and photocatalysis, Energy Environ. Sci. 5 (2012) 6717–6731.

[10] X. Chen, P. Tan, B. Zhou, H. Dong, J. Pan, X. Xiong, A green and facile strategy for preparation of novel and stable Cr-doped $SrTiO_3$/g-C_3N_4 hybrid nanocomposites with enhanced visible light photocatalytic activity, J. Alloy. Compd. 647 (2015) 456–462.

[11] W. Ho, Z. Zhang, W. Lin, S. Huang, X. Zhang, X. Wang, Y. Huang, Copolymerization with 2,4,6-triaminopyrimidine for the rolling-up the layer structure, tunable electronic properties, and photocatalysis of *g*-C_3N_4, ACS Appl. Mater. Interfaces 7 (2015) 5497–5505.

[12] S. Xu, P. Zhou, Z. Zhang, C. Yang, B. Zhang, K. Deng, S. Bottle, H. Zhu, Selective oxidation of 5-hydroxymethylfurfural to 2,5-furandicarboxylic acid using O_2 and a photocatalyst of co-thioporphyrazine bonded to *g*-C_3N_4, J. Am. Chem. Soc. 139 (2017) 14775–14782.

[13] C. Ye, J.-X. Li, J.-Z. Li, X.-B. Li, X.-B. Fan, L.-P. Zhang, B. Chen, C.-H. Tung, L.-Z. Wu, Enhanced driving force and charge separation efficiency of protonated *g*-C_3N_4 for photocatalytic O_2 evolution, ACS Catal. 5 (2015) 6973–6979.

[14] Y. Shang, X. Chen, W. Liu, P. Tan, H. Chen, L. Wu, C. Ma, X. Xiong, J. Pan, Photocorrosion inhibition and high-efficiency photoactivity of porous *g*-C_3N_4/Ag_2CrO_4 composites by simple microemulsion assisted co- precipitation method, Appl. Catal. B 204 (2017) 78–88.

[15] Y. Deng, L. Tang, C. Feng, G. Zeng, J. Wang, Y. Lu, Y. Liu, J. Yu, S. Chen, Y. Zhou, Construction of plasmonic Ag and nitrogen-doped graphene quantum dots codecorated ultrathin graphitic carbon nitride nanosheet composites with enhanced photocatalytic activity: full-spectrum response ability and mechanism insight, ACS Appl. Mater. Interfaces 9 (2017) 42816–42828.

[16] Z. Zhao, Y. Sun, F. Dong, Graphitic carbon nitride based nanocomposites: a review, Nanoscale 7 (2015) 15–37.

[17] J. Zhu, P. Xiao, H. Li, S.A.C. Carabineiro, Graphitic carbon nitride: synthesis, properties, and applications in catalysis, ACS Appl. Mater. Interfaces 6 (2014) 16449–16465.

[18] X. Wang, K. Maeda, A. Thomas, K. Takanabe, G. Xin, J.M. Carlsson, K. Domen, M. Antonietti, A metal-free polymeric photocatalyst for hydrogen production from water under visible light, Nat. Mater. 8 (2009) 76–80.

[19] L. Jing, R. Zhu, D.L. Phillips, J.C. Yu, Photocatalysis: effective prevention of charge trapping in graphitic carbon nitride with nanosized red phosphorus modification for superior photo(electro)catalysis, Adv. Funct. Mater. 27 (2017) 1770277.

[20] Y.-N. Liu, C.-C. Shen, N. Jiang, Z.-W. Zhao, X. Zhou, S.-J. Zhao, A.-W. Xu, *g*-C_3N_4 hydrogen bonding viologen for significantly enhanced visible light photocatalytic H_2 evolution, ACS Catal. 7 (2017) 8228–8234.

[21] Q. Zhang, S. Yang, S.-N. Yin, H. Xue, Over two-orders of magnitude enhancement of the photocatalytic hydrogen evolution activity of carbon nitride via mediator-free decoration with gold-organic microspheres, Chem. Commun. 53 (2017) 11814–11817.

[22] R.P. Sabatini, T.M. McCormick, T. Lazarides, K.C. Wilson, R. Eisenberg, D.W. McCamant, Intersystem crossing in halogenated bodipy chromophores used for solar hydrogen production, J. Phys. Chem. Lett. 2 (2011) 223–227.

[23] F. Song, H. Zhang, D.-G. Wang, T. Chen, S. Yang, G.-C. Kuang, Imine-linked porous organic polymers showing mesoporous microspheres architectures with tunable surface roughness, J. Polym. Sci. Part A Polym. Chem. 56 (2018) 319–327.

[24] D.-G. Wang, F. Song, H. Tang, X.-R. Jia, M. Song, G.-C. Kuang, A facile route to prepare dimeric BODIPY-based porous organic polymers using $FeCl_3$, New J. Chem. 41 (2017) 5263–5266.

[25] Y. Zhu, Y.-J. Ji, D.-G. Wang, Y. Zhang, H. Tang, X.-R. Jia, M. Song, G. Yu, G.-C. Kuang, BODIPY-based conjugated porous polymers for highly efficient volatile iodine capture, J. Mater. Chem. A 5 (2017) 6622–6629.

[26] D.-G. Wang, L.-N. Zhang, Q. Li, Y. Yang, Y. Wu, X. Fan, M. Song, G.-C. Kuang, Dimeric BODIPYs with different linkages: a systematic investigation on structure-properties relationship, Tetrahedron 73 (2017) 6894–6900.

[27] H. Wang, Y. Wu, Y. Shi, P. Tao, X. Fan, X. Su, G.-C. Kuang, BODIPY-based fluorescent thermometer as a lysosome-targetable probe: how the oligo(ethylene glycols) compete photoinduced electron transfer, Chem. Eur. J. 21 (2015) 3219–3223.

[28] H. Wang, Y. Wu, P. Tao, X. Fan, G.-C. Kuang, BODIPY-based oligo(ethylene glycol) dendrons as fluorescence thermometers: when thermoresponsiveness meets intramolecular electron/charge transfer, Chem. Eur. J. 20 (2014) 16634–16643.

[29] A. Loudet, K. Burgess, BODIPY dyes and their derivatives: synthesis and spectroscopic properties, Chem. Rev. 107 (2007) 4891–4932.

[30] D.J. Martin, K. Qiu, S.A. Shevlin, A.D. Handoko, X. Chen, Z. Guo, J. Tang, Highly efficient photocatalytic H_2 evolution from water using visible light and structure-controlled graphitic carbon nitride, Angew. Chem. Int. Ed. 53 (2014) 9240–9245.

[31] X. Chen, H. Li, Y. Wu, H. Wu, L. Wu, P. Tan, J. Pan, X. Xiong, Facile fabrication of novel porous graphitic carbon nitride/copper sulfide nanocomposites with enhanced visible light driven photocatalytic performance, J. Colloid Interface Sci. 476 (2016) 132–143.

[32] X. Chen, B. Zhou, S. Yang, H. Wu, Y. Wu, L. Wu, J. Pan, X. Xiong, In situ construction of an SnO_2/*g*-C_3N_4 heterojunction for enhanced visible-light photocatalytic activity, RSC Adv. 5 (2015) 68953–68963.

[33] Y. Chen, B. Wang, S. Lin, Y.F. Zhang, X. Wang, Activation of n→π* transitions in two-dimensional conjugated polymers for visible light photocatalysis, J. Phys. Chem. C 118 (2014) 29981–29989.

[34] W. Ho, Z. Zhang, W. Lin, S. Huang, X. Zhang, X. Wang, Y. Huang, Copolymerization with 2, 4, 6-triaminopyrimidine for the rolling-up the layer structure, tunable electronic properties and photocatalysis of *g*-C_3N_4, ACS Appl. Mater. Interfaces 7 (2015) 5497–5505.

[35] P. Tan, X. Chen, L. Wu, Y. Shang, W. Liu, J. Pan, X. Xiong, Hierarchical flower-like $SnSe_2$ supported Ag_3PO_4 nanoparticles: towards visible light driven photocatalyst with enhanced performance, Appl. Catal. B 202 (2017) 326–334.

[36] X. Fan, L. Zhang, M. Wang, W. Huang, Y. Zhou, M. Li, R. Cheng, J. Shi, Constructing carbon-nitride-based copolymers via Schiff base chemistry for visible-light photocatalytic hydrogen evolution, Appl. Catal. B 182 (2016) 68–73.

[37] R.A.C. Amoresi, V. Teodoro, G.F. Teixeira, M.S. Li, A.Z. Simões, L.A. Perazolli, E. Longo, M.A. Zaghete, Electrosteric colloidal stabilization for obtaining $SrTiO_3$/TiO_2 heterojunction: microstructural evolution in the interface and photonics properties, J. Eur. Ceram. Soc. 38 (2018) 1621–1631.

[38] P.F.S. Pereira, A.F. Gouveia, M. Assis, R.C. de Oliveira, I.M. Pinatti, M. Penha, R.F. Goncalves, L. Gracia, J. Andres, E. Longo, $ZnWO_4$ nanocrystals: synthesis, morphology, photoluminescence and photocatalytic properties, Phys. Chem. Chem. Phys. 20 (2018) 1923–1937.